Nanoscale

PAPER

View Article Online
View Journal

Cite this: DOI: 10.1039/d5nr04879f

Supported high- and medium-entropy nanoalloys from MOFs catalyze the alkene oxidation reaction

Alejandro Lumbreras-Teijeiro,[a] Anna Nowacka,[a] Alejandro Serrano-Maldonado,[a] Matthijs A. van Spronsen,[b] Judit Oliver-Meseguer *[a] and Antonio Leyva-Pérez *[a]

Received 18th November 2025,
Accepted 22nd May 2026

DOI: 10.1039/d5nr04879f

rsc.li/nanoscale

High- and medium-entropy alloys (HMEAs) are emerging as promising catalysts due to their different electronics and very good thermal stability. HMEAs have already exhibited remarkable catalytic performance in several electrocatalytic reactions involving small molecules; however, their use in thermal complex organic reactions is still in its infancy. Herein, we present a highly dense supported HMEA material (≈50 wt% in metal) prepared by the pyrolysis of a metal–organic framework (MOF), used as a template in virtue of its well-spaced single metal atoms, to obtain catalytic carbon-supported nano-HMEAs in a particle-to-particle synthetic way. The solid material shows a remarkable catalytic activity for alkene oxidation reactions and can be recycled at least 10 times; however, a higher activity of the monometallic catalysts in terms of the turnover number is found. These results constitute, to our knowledge, one of the first examples of catalytic HMEAs for organic synthesis.

Introduction

Metals are of such social and historical significance that two eras are named after them, the Iron Age and the Bronze Age (as an alloy, bronze was the first truly engineered material).[1] Alloys began with one and rarely two principal elements, such as iron in steel or nickel in superalloys, with enhanced properties. However, despite the fact that humans have developed new alloys with metals since ancient times, it was about two decades ago when a new promising alloy design was proposed, involving mixing of multiple elements in an equimolar or near-equimolar composition.[2–6] These designed multicomponent alloys were termed 'high-entropy alloys' (HEAs) by Yeh *et al.*,[3] which describes the high configurational entropy after the random mixing of metal elements. In the early days, HEAs were limitedly defined as alloys composed of five or more elemental components in equimolar ratios. Nowadays, medium-entropy alloys (MEAs) with 3–5 elements are also considered and, in both cases (HEAs and MEAS, *i.e.* HMEAs), the properties are significantly regulated by tuning the metallic component.[7] Unlike conventional metal alloys, which contain one and rarely two base metal elements, HMEAs comprise multiple principal elements, with the number of HMEA compositions extending considerably to more than conventional alloys, and this metal combination not only regulates the electronic and geometric structures to a large degree but also serves as a platform to construct catalysts with unexpected performance.[8–16]

The use of nanoparticles (NPs) is preferred with respect to macroscopic metals in catalysis, since the high surface-to-volume of the former enables a higher interaction with external reactants. In view of this, a variety of strategies has been proposed to produce HMEA NPs, such as mechanical ball milling, plasma arc discharge, ultrasonication, deposition, fast moving bed pyrolysis and chemical methods involving carbothermal shock, hydrothermal, and solvothermal reactions.[17–24] However, these methods are often tedious and tend to produce a wide distribution of NP sizes. Here, we use a pre-formed, well-defined multimetallic metal–organic framework (MOF) as a template, a strategy rarely seen in the synthesis of catalytic HMEA NPs.

MOFs are micro-structured solid materials that consist of organic linkers and metal centres, to form three-dimensional crystalline structures, as shown in Scheme 1.[25,26] The careful choice of these components enables a flexible structure design with well-defined pore sizes, surface area and functionalities. All of these properties make MOFs extremely advantageous not only in their use as a pure material or as a support for single atom or small cluster metal catalysts,[27,28] but also as a sacrificial precursor for other hybrid inorganic–organic nanostructures.[29] Particularly, the metal atoms in the crystal lattice and the organic linkers constitute a source of metal NPs and

[a]Instituto de Tecnología Química, Universitat Politècnica de València-Agencia Estatal Consejo Superior de Investigaciones Científicas, Avda. de los Naranjos s/n, 46022 València, Spain. E-mail: anleyva@itq.upv.es, joliverm@itq.upv.es
[b]Diamond Light Source Ltd, Harwell Science and Innovation Campus, Chilton, Didcot, OX11 0DE, UK

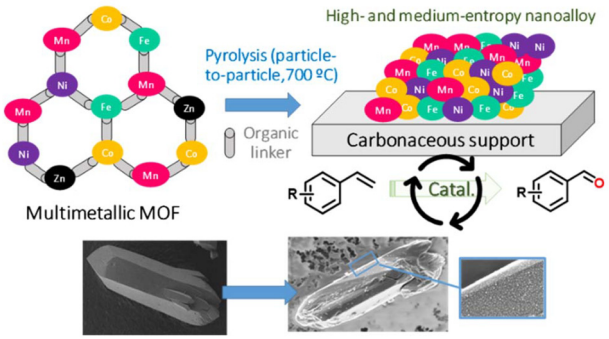

Scheme 1 Synthesis of the supported high- and medium-entropy alloy (HMEA) nanoparticles reported in this work, starting from a multimetallic metal–organic framework (MOF) and catalysing the oxidative breaking of styrenes to benzaldehydes, with microscopy images of the particle (MOF)-to-particle (HMEA) synthesis.

microporous carbon, respectively, when properly pyrolyzed.[30–32] In other words, MOFs drive the manufacture of entropy-driven materials such as multi-metal oxides, metal carbides and sulphides, among others,[33] which cannot be synthesized following traditional approaches. Thanks to the previous construction of a MOF, the metal clusters coordinated by organic linkers effectively prohibit the agglomeration of the resultant metal NPs, providing a homogeneous distribution over the support after pyrolysis.[34]

MOFs were reported as a template for metal-supported carbonaceous materials in 2008[35] and, since that time, many variations of MOF material precursors and procedures have been developed. Just to mention a couple of examples, Co/C catalysts were synthesized by well controlled pyrolysis of ZIF-67 above 450 °C,[36] and other examples followed. Based on different characterization methods, Co/C catalysts were confirmed to possess Co° entrapped in a carbon matrix, polished by a certain amount of pyridinic and graphitic N and a small portion of adsorbed oxygen, and these NPs were evaluated in the Fischer–Tropsch reaction. More recently, MOF based Cu–Pt bimetallic nanoparticles supported on a nonporous carbon composite were prepared after using a slightly different approach.[37] The method involved carbonization of Cu–MOF-199 under a N_2 atmosphere at 900 °C followed by partial galvanic replacement of Cu by Pt^{IV} ions upon immersion in a hexachloroplatinic acid solution. The good performance of the alloy for the hydrogen evolution reaction (HER) was attributed to the synergetic effect of the Cu and Pt metals, with uniform distribution of the Pt nanoparticles over the surface. The flexibility of the MOF structure allowed the introduction of more than one metal into the lattice, in order to construct multi-metal MOFs to tune its properties,[38] and it is now accepted that the use of multi-metal MOFs as a template can yield alloy metal NPs with intrinsic characteristics. As compared to mono- or bi-metallic NPs, multimetallic NPs with controlled composition and size may exhibit distinct catalytic activity during the reaction due to the metal–metal interactions on the alloy catalysts.[39,40] For example, bi- and trimetallic Co, Ni and Cu alloy nanoparticles have been prepared after the pyrolysis of the corresponding mulimetallic MOF under an inert atmosphere, to obtain highly dispersed and embedded metal NPs.[41] Despite many reported examples of the use of MOF-driven alloy NPs, the synthesis of HMEAs from MOFs is still basically unknown since it requires construction and pyrolysis of MOFs of at least 5 different metal atoms, to create the basis for the supported HMEAs. In fact, MOFs are often limited to two to three metals,[41–45] and the simultaneous control over both the composition and the size of HMEA NPs remains a challenge, and the crucial interplay between the size, composition and atomic structure of these new nanosystems has hardly been addressed from MOFs.[46]

Scheme 1 shows our approach reported here, which involves a simple particle-to-particle procedure to obtain a carbon matrix decorated with a high density of HMEA NPs (*ca.* 50 wt%), after the pyrolysis of a multimetallic MOF, and its catalytic activity in alkene oxidation reactions. To our knowledge, this is the first time that HMEA based materials are applied as catalysts to oxidation reactions since, in general, HMEAs are applied to hydrogenation reactions.[47–49] Indeed, HMEAs are recognized as potential catalysts for a variety of reactions,[17,50–54] but their use in conventional thermal organic synthesis is still minor compared to that in electrochemical processes,[55–58] the former being relegated to mainly computational studies.[59,60]

Results and discussion

Synthesis and characterization of the HMEA precursor MOF 1 (Ni, Co, Fe, Mn, and Zn)

In order to prepare a well-dispersed multimetallic MOF, we modified a described procedure for MOF-74,[61] using nitrate salts of Ni, Co, Zn and Mn, and Fe sulphate as metal sources (see the experimental procedures in the SI, SM, for more information).

The selection of a modified MOF-74 was based on its ability to accommodate up to ten different metals in the framework, with high metal content, and the presence of volatile Zn atoms in the material, which may help us to get unsaturated metal NPs with enhanced catalytic properties.[62–64] With this idea in mind, several batches of the penta-metallic MnCoFeNiZn MOF **1** were synthesized and characterized. Powder X-ray diffraction (PXRD) measurements were firstly carried out in order to confirm the robustness of the process, and Fig. 1 (top) shows the resulting patterns for one of the batches (see Fig. S1 for a three batch comparison), which matched the simulated MOF-74 powder PXRD pattern. It is worth commenting here that the simulated pattern is obtained for pure crystalline samples; thus only the peak position but not the intensity is expected to match (the intensity of the PXRD peaks can vary depending on the morphology of the sample, the crystallinity degree, the sample orientation and the grinding, among others). None or very little impurities present in the different spectra suggest good incorporation of the different metals

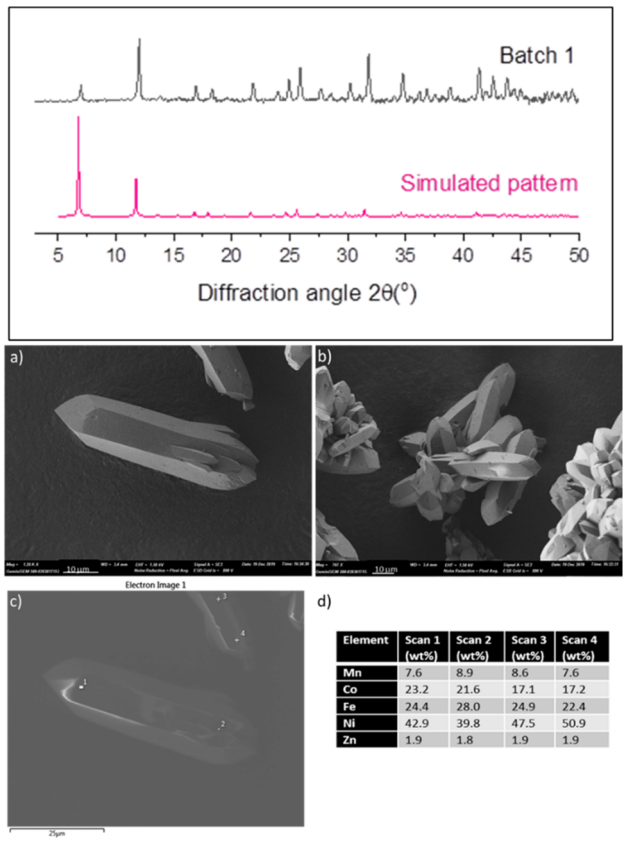

Element	Scan 1 (wt%)	Scan 2 (wt%)	Scan 3 (wt%)	Scan 4 (wt%)
Mn	7.6	8.9	8.6	7.6
Co	23.2	21.6	17.1	17.2
Fe	24.4	28.0	24.9	22.4
Ni	42.9	39.8	47.5	50.9
Zn	1.9	1.8	1.9	1.9

Fig. 1 Top: Diffraction patterns of the MOF **1** batch 1, compared with the simulated pattern. Bottom: (a and b) Field emission scanning electron microscopy (FESEM) images of MOF **1** (batch 1); (c and d) representative energy-dispersive X-ray spectroscopy (EDS) analysis of MOF **1** crystals in batch 1, at four different locations (scans 1–4). The peak observed at 8° is due to an impurity.

inside the MOF **1** lattice. Anyway, it has to be said that the fact that no other signals are present does not necessarily mean that other phases are not present, but that they might be amorphous.

The amount and percentage of each metal in the different batches were determined by inductively coupled plasma optical emission spectroscopy (ICP–OES, Table S1). Notice here that the wt%, at% and mol% values for the metals practically coincide since all metal atoms are neighbouring elements of the first transition raw in the Periodic Table. It is true that the ICP–OES values for each metal differ somewhat from batch to batch (not more than 15%); however, considering the complexity of forming the multimetallic MOF and that the variation in initial metal content and proportions does not have a significant influence, neither in the final HMEA structure nor the catalytic behaviour (the metal content from nanoparticle to nanoparticle and the catalytic activity are quite similar, in average, see ahead), we can accept these variations within a reasonable limit.

The morphology and microstructure of the as-synthesized MOF **1** samples were investigated using field emission scanning electron microscopy (FESEM) and energy-dispersive X-ray analysis (EDX), as shown in Fig. 1 (bottom). All crystals presented the same morphology with average crystal size around 50 μm (Fig. 1a and b), and the metal content according to EDX was acceptably similar to that from the ICP–OES analysis for each batch, except for Zn, which showed lower values (Fig. 1c and d). This result may reveal that Zn easily sublimates under the electron beam, independent of its location in the crystal.[65,66]

A thermogravimetry differential thermal analysis (TG/DTG) of MOF **1** shows two major weight-loss steps (Fig. S2). The first weight loss takes place at 25–100 °C, which corresponds to the elimination of adsorbed and volatile water and guest solvent molecules, with a value around 24 wt%, also confirmed by differential scanning calorimetry (DSC). Then, small mass changes in the range 180–200 °C occur, which might indicate the presence of DMF guest molecules, due to insufficient methanol exchange time after synthesis. Finally, complete decomposition of the organic material in MOF **1** is observed at 330 °C, the remaining mass fitting the expected weight of metals. These data allowed us to estimate the minimum temperature for the pyrolysis procedure. The surface area of the precursor MOF **1** is lower than that expected for MOFs (294.1 m^2 g^{-1}). The low surface area obtained for the MOF **1**, compared to the typical ones obtained for these materials, can be attributed to the mild reaction conditions for washing and drying (see the reaction procedures in the SI), which fail to achieve complete removal of guest molecules, leading to pore blockage and the presence of impurities. However, the area of HMEA-700 is 274 m^2 g^{-1}, similar to that of the precursor, and is thus favourable for the synthetic approach.

Synthesis and characterization of the carbon-supported HMEA NPs (Ni, Co, Fe, and Mn)

The decomposition temperature of MOF **1** serves as a starting point to study the formation of the HMEA NPs. Fig. 2 shows the PXRD of MOF **1** after pyrolysis, at 400 °C, 550 °C, 700 °C and 800 °C, during 4 h under a flow of N_2 gas. Nearly complete decomposition of the pristine MOF **1** could be already seen at

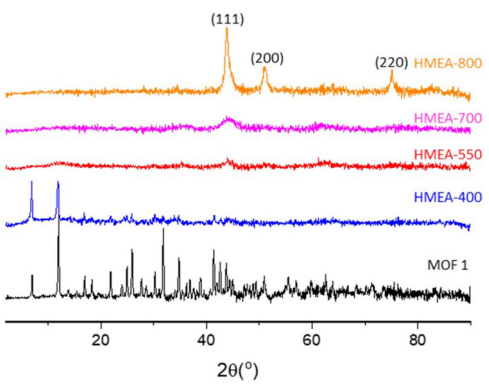

Fig. 2 Diffraction patterns (PXRD) of the MOF **1** sample pyrolyzed at increasing temperatures, compared to the as-prepared MOF **1** (bottom).

400 °C, as assessed from the disappearance of the diffraction peaks in the corresponding PXRD patterns; this sample was thereafter named HMEA-400 for the sake of clarity. When the pyrolysis temperature was increased to 550 °C, new but small diffractions at $2\theta = 44°$, 51° and 75° were observed. These diffraction peaks can be attributed to the (111), (200) and (220) lattice planes of metal alloy particles with a face centred cubic (FCC) structure, a very common phase for HEAs,[10] and their signals continuously intensified on increasing the temperature to 700 °C and 800 °C. Nevertheless, they remained broad, and the Scherrer equation gave values of <10–20 nm (9.7 nm, considering a shape factor = 0.9). No peak was observed at ~26°, indicating that the organic linkers from MOFs turned amorphous and not into any kind of crystalline carbon.

Subsequently, materials pyrolyzed at all tested temperatures, except at 800 °C, subsequently underwent reduction under H_2 (100 mL min^{-1}) at 400 °C for 4 h. We then examined all the reduced samples by FESEM to track morphological changes in the material, caused by the modification in pyrolysis temperature (Fig. 3). With pyrolysis at 400 °C (Fig. 3A), the material shows a smooth surface with some alloy NPs appearing in an irregular manner, and with a wide particle size distribution centred around ~16 nm (Fig. S3). This result is in accordance with the TG/DTG and PXRD analysis results, since the organic components of MOF **1** start to decompose at this temperature. The situation dramatically changed when the material was pyrolyzed at 550 °C, and the resulted sample HMEA-550 (Fig. 3B) shows more regular and abundant metal NPs (average size ~18 nm; see Fig. S4), with the formation of a nanoporous carbon structure having some cracks along the particle. Increasing the pyrolysis temperature further up to 700 °C enabled an optimum distribution of metal NPs (Fig. 3C, see also Fig. S5 and S6).

The sample HMEA-700 contains spherical NPs, equally dispersed and covering all the nanoporous carbon surface, with a very narrow particle size distribution centred around 11 nm (Fig. S5), a significantly smaller size than those of the materials pyrolyzed at 400 °C and 550 °C. At 800 °C (Fig. 3D), the material shows a defined structure but with bigger NPs (~30 nm) and a wider size distribution also (see also Fig. S6). For all the carbonized materials, the same morphology of the parent MOF **1** can be observed, which indicates that the chemical transformation of MOF **1** occurs intraparticle during the pyrolysis process (see Fig. S7 with HMEA-550 as a representative example).[67] The conversion of the organic linkers into a carbon matrix should act as a reducing process for the metal cations, thus developing a carbon-supported multi-metal hybrid nanomaterial after complete pyrolysis of the organic part.

Fig. 3F–G show the metal content in HMEA-700 according to ICP–OES analyses, and it can be seen that four of the metals (Mn, Co, Fe and Ni) are present in a similar ratio (*ca.* 15–20 wt% each), while Zn mainly disappeared. The examination of individual NPs was then accomplished by HR–STEM coupled with energy-dispersive X-ray (EDX) spectroscopy, and the results (see Fig. S8) also show that most of the NPs in HMEA-700 exhibit a similar chemical composition: *i.e.*, $Fe_{29}Ni_{45}Co_{22}Mn_4$, $Fe_{31}Ni_{38}Co_{24}Mn_6$, $Fe_{27}Ni_{43}Co_{24}Mn_7$, and $Fe_{42}Ni_{326}Co_{29}Mn_3$. However, a detailed speciation by TEM and STEM analyses shows that some NPs in the HMEA-700 sample are Ni-richer and others are Fe-richer (Fig. S8e). The Ni content determined by ICP–OES is lower compared to that from EDX since the latter somehow shows the composition near or at the surface of the sample and, as XPS measurements denote, Ni tends to be enriched on the surface of the NPs. The lack of Zn, also observed when analyzing the MOF **1** sample by FESEM (Fig. 1), can be explained by the sublimation of this metal, with a much lower melting point (419.5 °C), compared to those of Fe (1538 °C), Ni (1455 °C), Co (1495 °C) and Mn (1246 °C). This low melting point might have provoked leaching of Zn out of the material during the pyrolysis procedure, resulting in its deposition at the exhaust of the reactor, a phenomenon well-known in alloyed NP synthesis to enhance the catalytic properties of the materials.[64,68]

Another change in the chemical composition of the NPs with respect to the MOF **1** predecessor is the lower amount of Mn in the NP but not in the overall metal content of the material, which cannot be explained by a potential sublimation. A closer look at the HMEA-700 sample by HR-TEM showed the presence of Mn-rich NPs ($Fe_1Co_1Mn_{98}$) after

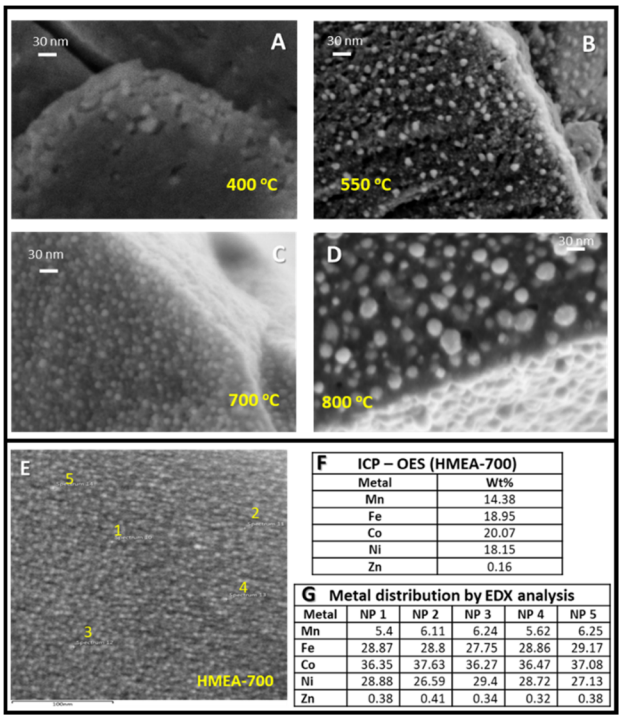

F ICP – OES (HMEA-700)

Metal	Wt%
Mn	14.38
Fe	18.95
Co	20.07
Ni	18.15
Zn	0.16

G Metal distribution by EDX analysis

Metal	NP 1	NP 2	NP 3	NP 4	NP 5
Mn	5.4	6.11	6.24	5.62	6.25
Fe	28.87	28.8	27.75	28.86	29.17
Co	36.35	37.63	36.27	36.47	37.08
Ni	28.88	26.59	29.4	28.72	27.13
Zn	0.38	0.41	0.34	0.32	0.38

Fig. 3 Field emission scanning electron microscopy (FESEM) images of the resulting materials after pyrolyzing MOF **1**: at (A) 400 °C (5 °C min^{-1}), (B) 550 °C (5 °C min^{-1}), (C) 700 °C (5 °C min^{-1}), and (D) 800 °C (10 °C min^{-1}) for 5 h. (E) HR–FESEM picture of HMEA-700 with ICP–OES analysis (F), and the metal distribution according to energy-dispersive X-ray (EDX) spectroscopy analysis of individual NPs (G) indicated in image E. Pyrolysis at all temperatures except at 800 °C was followed by reduction in H_2 (100 mL min^{-1}) at 400 °C for 4 h.

measuring more individual NPs (Fig. S8a and S9f), which explains this decrease in Mn in the supported HMEA NPs. It is worth commenting here that no Zn-rich NP could be found. In order to confirm the formation of Mn-rich NPs in HMEA–700, carbon-supported Mn NPs were prepared by impregnation of active charcoal with $Mn(NO_3)_2{\cdot}4H_2O$ and reduced under H_2 (100 mL min^{-1}) at 400 °C for 4 h (see the Experimental section for details). The corresponding PXRD pattern confirms the formation of Mn NPs in the HMEA-700 material after H_2 reduction (Fig. S10).

The HMEA-800 solid shows a similar composition of the NPs as in HMEA-700, *i.e.*, $Fe_{50}Ni_{25}Co_{22}Mn_3$, $Fe_{54}Ni_{22}Co_{21}Mn_3$, $Fe_{58}Ni_{25}Co_{15}Mn_2$, and $Fe_{56}Ni_{27}Co_{15}Mn_2$ (Fig. S11). A similar amount of Mn and the absence of Zn persist at 800 °C. Fast Fourier transform (FFT) patterns of selected HMEA NPs in HMEA-800 show a FCC structure for the alloyed NP, also recognizable in the corresponding PXRD patterns (see also Fig. 2 and Fig. S11). This FFC structure is also visible in the NPs of the HMEA-700 materials before H_2 reduction (see Fig. 2), but not in the nascent NPs in HMEA-400 and HMEA-550, since it is not until 700 °C when true crystalline HMEA NPs in the pure FCC phase are clearly formed.[69]

Individual NPs of the HMEA-550, HMEA-700 and HMEA-800 materials were then compared (please note that the HMEA-400 material still shows ill-defined NPs) and Fig. 4 shows that the amounts of Zn and Mn are roughly the same for HMEA-550 in 12 different examined NPs (see also Fig. S12). Mn is the major metal component (>35 wt%) and the Zn amounts are significantly higher than those in other NPs (>10 wt%), which indicates that Mn forms individual NPs and Zn sublimates at 550 °C, concomitantly, and that these two effects could be chemically related since these early formed Mn-rich NPs contain significant amounts of Zn. In contrast, HMEA-700 (Fig. 3E and G) shows that the amount of each metal is similar in all the NPs examined, being lower than 7 wt% for both Mn and Zn. Indeed, only after Zn disappears, the solid material starts to be catalytically active (see ahead). All these results come from different MOF batches, which we consider statistically acceptable for the final application (catalysis), thus being scientifically sounder than just one single "successful" batch.

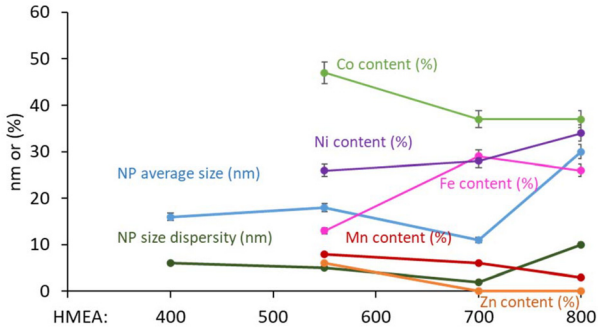

Fig. 4 Comparison of the NP size, dispersity, and metal relative content for the different HMEA-supported materials obtained by energy-dispersive X-ray (EDX) spectroscopy. Error bars account for a 5% uncertainty.

All the above results strongly support that the HMEA NPs formed from MOF **1** are composed of similar amounts of Co, Fe and Ni (~20 wt%), with lower amounts of Mn (~5 wt%), remaining stabilized on amorphous carbon after hydrogenation and pyrolysis of MOF **1** at a temperature of ~700 °C. In this way, densely distributed HMEA NPs (nearly 50 wt% in total metal content) with good size distribution (11 ± 2 nm average particle size) can be obtained. Based on the definition for HEAs and MEAs (Fig. S13 in the SI), we must consider the material here reported as a high- and medium-entropy alloy, since HMEAs refer to the alloys composed of three or more elemental components, with the concentration of each element being between 5 and 35 atomic percentage (at%).[10–13]

In situ characterization during the MOF 1 pyrolysis

This study presents our first example of an HMEA synthesized *via* this method. We aim to understand its formation, metal distribution, and nature to improve its preparation and explore its catalytic applications. For this purpose, we employed *in situ* techniques. X-ray-based spectroscopy techniques, such as XAS and XPS, are powerful methods for studying catalysts. XAS, including XANES, provides information on the elemental composition and oxidation states and is well-suited for *in situ* and *operando* studies. XPS, a surface-sensitive technique, reveals surface composition and chemical states but has limitations under high pressure due to photoelectron scattering. This challenge is addressed by ambient-pressure XPS (AP-XPS), which extends XPS capabilities to more realistic conditions using synchrotron radiation. AP-XPS enables detailed analysis of surface chemistry and active phases during reactions, often providing insights not accessible through *ex situ* methods.

The oxidation state of the individual elements in the different HMEA samples obtained after reduction in H_2 was studied using X-ray photoelectron spectroscopy (XPS). For this analysis, the HMEA samples were exposed to H_2 at different temperatures (100, 200, 300, and 400 °C) in the XPS prechamber, followed by vacuum evacuation of the gas, ensuring that any contact with air does not occur before the measurement. These analyses (Fig. S14) also provide a qualitative assessment of the relative amounts of each metal on the surface of the sample after reduction at different temperatures. High-resolution Co 2p XPS spectra of the fresh and reduced samples exhibit asymmetric peaks. This asymmetry can be attributed to the presence of two main contributions at approximately 784 and 779 eV, corresponding to oxidized Co^{2+} and metallic Co^0 species, respectively. Due to the limited spectral resolution, quantitative deconvolution of these contributions is not reliable. However, a shift of the main band from 778.3 to 777.7 eV is observed with increasing reduction temperature, which is indicative of alloy formation with less electronegative elements such as Fe or Mn.[70] The Fe 2p high-resolution XPS spectrum of the fresh sample shows three peaks at 707.1, 710.9, and 715.5 eV, corresponding to Fe^0, Fe^{2+}, and Fe^{3+} species, respectively. Upon reduction, the Fe^{3+} contribution disappears, and

Fe^{2+} remains the dominant species up to 300 °C. After reduction at 400 °C, the spectrum can be deconvoluted into two peaks at 707.8 and 706.0 eV, indicating the formation of more reduced Fe species. Overall, increasing the reduction temperature leads to a higher fraction of metallic iron. For Ni, two main peaks are observed in the fresh sample and in samples reduced at 200, 300, and 400 °C, located at 855.8 and 856.1 eV, which are assigned to Ni^0 and Ni^{2+} species, respectively. With increasing reduction temperature, these peaks shift toward lower binding energies, similar to the behaviour observed for Co, consistent with an alloy formation. In contrast, the sample reduced at 100 °C exhibits a single Ni peak at 854.7 eV, which does not follow the general trend observed for the other metals upon increasing reduction temperature. For Mn, the XPS results indicate that oxidized Mn species (~641 eV) remain stable at the surface across all reduction temperatures investigated. This suggests that Mn is not reduced under any of the applied H_2 treatment conditions. Overall, while Co and Ni are partially reduced to metallic and alloyed states at relatively low temperatures, Fe remains predominantly oxidized until reduction at 400 °C, and Mn remains oxidized regardless of the reduction treatment.

A deeper analysis was performed using near-ambient pressure (NAP) X-ray photoelectron spectroscopy and X-ray absorption spectroscopy (XAS) measurements (see the SI for details on sample preparation, instrumentation and data collection). All the elements in the outer several nanometres of the HMEA nanoparticles of the as-loaded sample, which had been annealed to 800 °C under vacuum, were oxidised (Fig. 5 and 6). In agreement with the previous characterisation techniques, the Zn $L_{2,3}$ edge was not observed (data not shown).

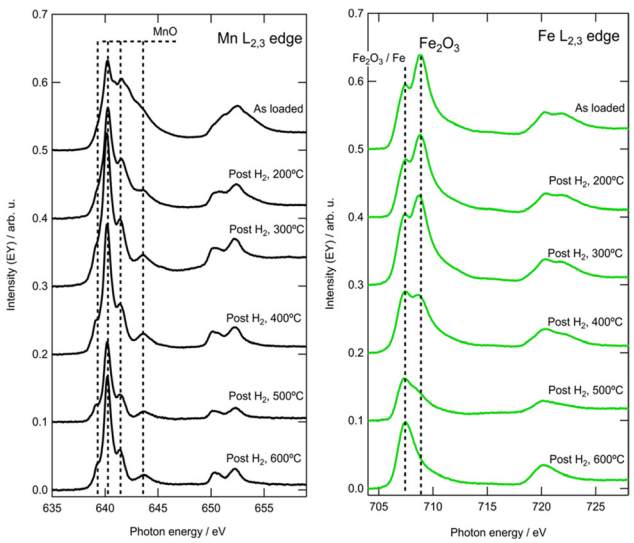

Fig. 5 X-ray absorption spectroscopy (XAS) spectra of Mn $L_{2,3}$ edges (left) and Fe $L_{2,3}$ edges (right) recorded under high vacuum at 22–37 °C, as-loaded and after the progressive anneal steps. Spectra are collected *via* electron yield, normalised to the I_{zero} signal, background subtracted, and offset for clarity. Dashed lines indicate features of the common oxides.

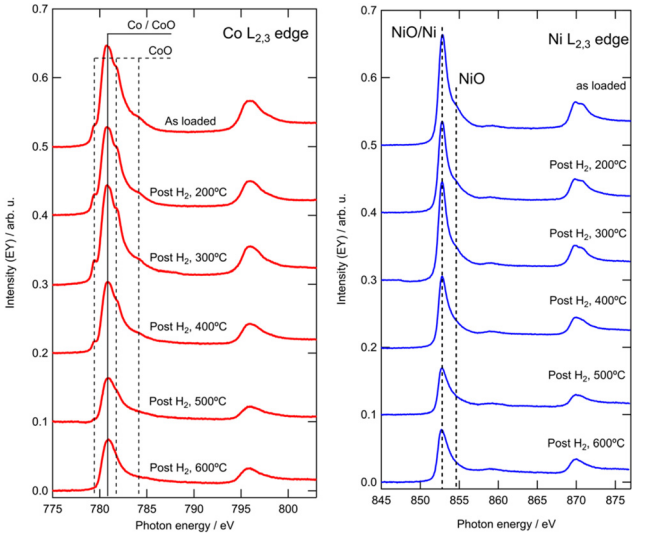

Fig. 6 X-ray absorption spectroscopy (XAS) spectra of Co $L_{2,3}$ edges (left) and Ni $L_{2,3}$ edges (right) recorded under high vacuum at 22–35 °C, as-loaded and after the progressive anneal steps. Spectra are collected *via* electron yield, normalised to the I_{zero} signal, background subtracted, and offset for clarity. Dashed lines indicate features of the common oxides.

Fig. 5 shows that manganese is originally present as a mixture of oxides (top spectrum, Fig. 5a). Mild annealing to 200 °C in H_2 is sufficient to drastically change the spectrum with the result resembling that of MnO. Further annealing does not lead to further changes and reduction beyond Mn(II). The spectrum obtained after annealing to 600 °C matched the earlier published spectra for MnO.[71] To quantify the intermediate spectra, the 600 °C spectrum was subtracted (after scaling), resulting in a spectrum that appears like that of Mn_3O_4. The Mn_3O_4/MnO ratio obtained was 3 (for the as-loaded sample) by measuring the relative edge jumps, describing an exponential drop, with hardly noticeable contribution from 500 °C onwards.

The Fe $L_{2,3}$ edges show that the initial spectrum is a combination of Fe and Fe_2O_3 (Fig. 5, right). The spectrum only starts to show visible changes after annealing to 400 °C. The final spectrum indicates fully reduced Fe. Focusing on the Fe_2O_3 : Fe ratio, we can observe that Fe_2O_3 reduction started after the first annealing step, generally following a linear trend. The initial ratio was 5 : 2, while the final spectrum did not show any contribution from Fe_2O_3.

Fig. 6 shows that the same measurements were performed for the Co $L_{2,3}$ and Ni $L_{2,3}$ edges, in order to analyse their reduction behaviour. The results indicate that achieving a fully reduced Co signal requires annealing at temperatures up to 500 °C (left). In contrast, the NiO band gradually diminishes and completely disappears after annealing at 400 °C, suggesting that Ni is more easily reduced under these conditions compared to Co.

The XPS analysis of the HMEA-800 sample shows that, apart from a gradual intensity attenuation, the C K edge spectra (Fig. S15) of the powder as-loaded and after the anneal-

ing steps are quite similar and resemble the previously reported spectra for graphite.

Near edge X-ray absorption fine structure (NEXAFS) spectra were then recorded (Fig. S16). The survey of the as-loaded HMEA-800 shows that most of the signal stems from carbon (C 1s at 248.9 ± 0.2 eV) and to much lesser extent from oxygen. Note that the photoionisation cross section of O 1s is roughly 3 times higher than that of C 1s at a photon energy of 1200 eV; therefore, the C 1s should be 3 times more intense. This C signal originates from the pyrolyzed organic linkers of the MOF, having become the support of the HMEA nanoparticles, while the latter could be located in the support and in oxidised HMEA nanoparticles. The O 1s peak position at 531.7 ± 0.2 eV and the FWHM of 4.8 eV suggest both cases. The spectra have clearly discernible features: (I) a strong peak assigned to the 1s → π* transition at 285.3 eV and a peak with a distinct shoulder (III and IV), which are typically assigned to 1s → σ* transitions. In between, there are contributions of states associated with the oxygenates, such as oxidised carbon or adsorbed water (II). With increasing annealing temperature, these species disappear, consistent with desorption/reduction. The intensity difference between levels below and above the absorption edge decreased with increasing annealing temperature, and this so-called edge jump is a quantitative measure of the amount of measured carbon.

The total edge jump, *i.e.*, the summed edge jumps of the four metals, showed a modest intensity decrease of around 30% with increasing annealing temperature. The NEXAFS spectra measured *via* electron yield are surface sensitive, probing the region within a few nanometres of the surface (see Fig. S16). So, the reduction in the total edge jump originates from a reduction of the total surface area of the HMEA particles. Because the as-loaded sample had already been annealed under vacuum to 800 °C, higher than that in *in situ* NEXAFS measurements, the surface area reduction can be linked to the H_2 atmosphere. In this way, an estimated average composition in the near surface region for the HMEA particles can be calculated, and the results shown in Fig. 7 indicate that the NP is enriched in Ni, as also observed by *ex situ* XPS analysis after the reduction processes (see Fig. S14). Overall, one can say that the composition of the HMEA-NP surface is a truly equimolar mixture of Mn, Fe, CO and Ni, somewhat enriched in the latter.

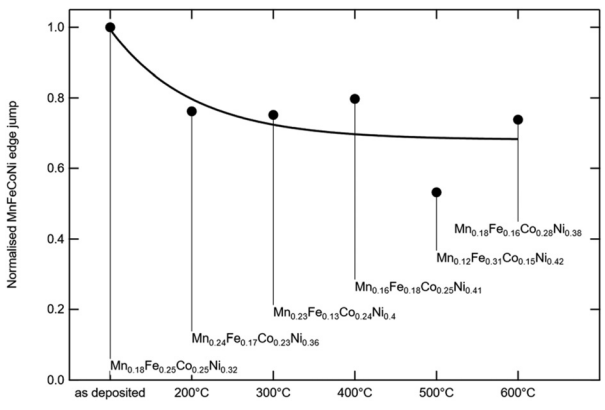

Fig. 7 Total edge jump of the HMEA sample and normalised to the as-loaded sample. An exponential fit is plotted to guide the eye. Molecular formulae give the average particle composition in the near surface region for all data points.

HMEA-700 as a heterogeneous catalyst for the alkene oxidation reaction

The small size and narrow distribution of the alloyed NPs in the HMEA-700 material, with a rather considerable surface/volume ratio, together with the high surface area obtained (274.5 $m^2\ g^{-1}$), prompted us to test this material as a catalyst for an organic reaction. We studied the oxidation of styrene **2a** with an excess of *t*-BuOOH **3** (3 equivalents), as shown in Fig. 8. This oxidation reaction requires the concomitant activation of the alkene and the peroxide on metal atoms.[72–74] Gratifyingly, complete conversion of **2a** to styrene epoxide **4a** and benzaldehyde **5a** was observed when using a 3 mol% of HMEA NPs, with a selectivity of **4a** : **5a** of 1 : 2.

The presence of Mn-rich NPs on the material raises the question of which types of NPs are actually responsible for the catalytic activity observed in HMEA-700 NPs for the styrene oxidation reaction (the FeCoNiMn NPs or the Mn NPs). In order to determine this, a batch of Mn NPs was synthesized by the impregnation methods (see Fig. S10 for characterization) and tested for the reaction. Fig. 8b and c show the calculated activation energy for the reaction (see also Fig. S17 for complete kinetics at different temperatures between 20 and 65 °C), and

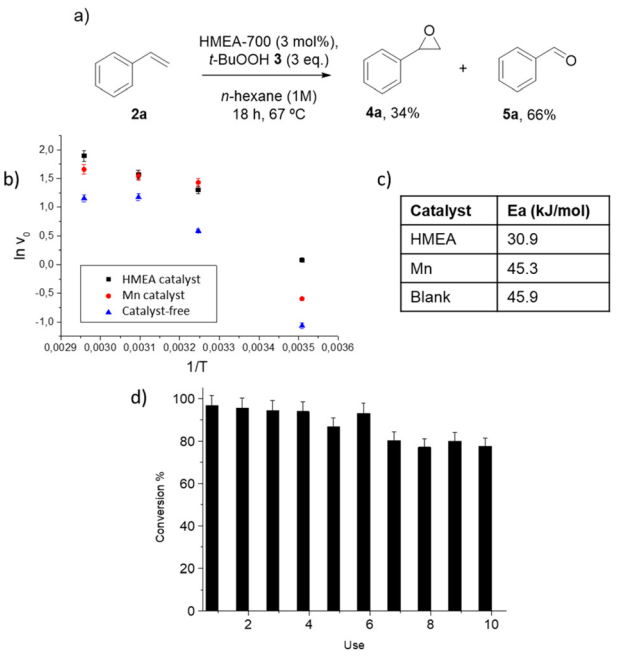

Catalyst	Ea (kJ/mol)
HMEA	30.9
Mn	45.3
Blank	45.9

Fig. 8 (a) Reaction scheme and first results for the oxidation of styrene **2a** with *t*-BuOOH **3** (3 equivalents) catalysed by HMEA-700 (3 mol%) in *n*-hexane as a solvent. (b) Arrhenius curves for the calculation of the activation energy for the HMEA catalyst, the Mn catalyst and a blank reaction. (c) Activation energies. (d) Reuses of the HMEA-700 solid catalyst. The selectivity of epoxide/aldehyde remains similar to that at the first use (see also Table S2). Error bars account for 5% uncertainty.

the Mn catalyst did not give any significant variation compared to the blank, while the HMEA solid presented a considerably lower activation energy (30.9 kJ mol^{-1}) with respect to the blank experiment (45.9 kJ mol^{-1}). Even at the highest temperature used, the initial rate of HMEA-700 is superior to that of Mn and blank tests strongly support that the FeCoNiMn NPs are actually the active species for the oxidation of styrene. Moreover, we also tested their stability by a hot filtration test, observing a minor activity from any leached species (Fig. S18). Any auto-oxidation process triggered by the catalyst in combination with the O_2 in the air can be excluded since the reaction occurs similarly to the blank experiment when the catalyst is removed. Besides, the oxidation of benzyl alcohol in the presence of HMEA-700 (3 mol%) under neat O_2 (3 atm) only gave an 8% conversion and a 5% yield of benzaldehyde **5a** after 78 h, discarding any O_2-triggered, free-radical autooxidation process (Fig. S19). Additionally, the oxidative cleavage of styrene **2a** in the presence of BHT as a free-radical scavenger was performed with yields around 90% with only 3 mol% of HMEA-700 (Fig. S20), corroborating that the reaction does not follow a free-radical pathway. In accordance, the reaction under a N_2 atmosphere gave the same result as that under air.

In accordance with the robustness of HMEA-700 and the lack of leaching during the reaction, Fig. 8d shows that the catalyst can be reused up to 10 times conserving most of the catalytic activity (with 78% conversion in the 10th use; see Table S2 for the selectivity results). It is true that a loss of 21% is significant; however, this is after 10 cycles, and thus a loss of 2.1% per reuse occurs in average, which might be considered acceptable for a complex supported metal catalyst under oxidizing reaction conditions. Indeed, the final conversion achieved after 10 times is still more than twice the conversion achieved without a catalyst (40%). Please note that the reuse experiment results at intermediate conversion will be close to that of the blank (40% conversion); thus the results might be confused with the blank and not be representative of the catalytic activity loss.

The catalytic results obtained for styrene **2a** were compared with previous results for the synthesis of the epoxide **4a** in the literature, under similar reaction conditions (Table S3).[75] It can be seen that the 82% yield of **4a** obtained is among the best results reported,[76–78] with the additional advantage that our catalyst here is easily recovered and reused. These results must be remarked on in the context of modern sustainable synthesis with supported metal nanoparticles.[79,80]

At this point, the scope of the oxidation reaction catalysed by the HMEA-700 solid was studied. It must be remarked here that the scope study was performed with 2.5 wt% of the solid catalyst, which accounts for ≈3 mol% of metals. Fig. 9 shows that a variety of styrene and allylbenzene derivatives **2a–g**, including terminal and internal alkenes, can undergo the oxidative cleavage reaction catalysed by HMEA-700, with moderate to high yields. In some cases, the selectivity of the reaction was very good, and the internal styrene **2c** gives the epoxide as the only product (**4c**), while Br and methoxy groups at the *para* position of the ring direct the reaction selectively to form the aldehyde products (**5f** and **5g**). The turnover number (TON) of the metal

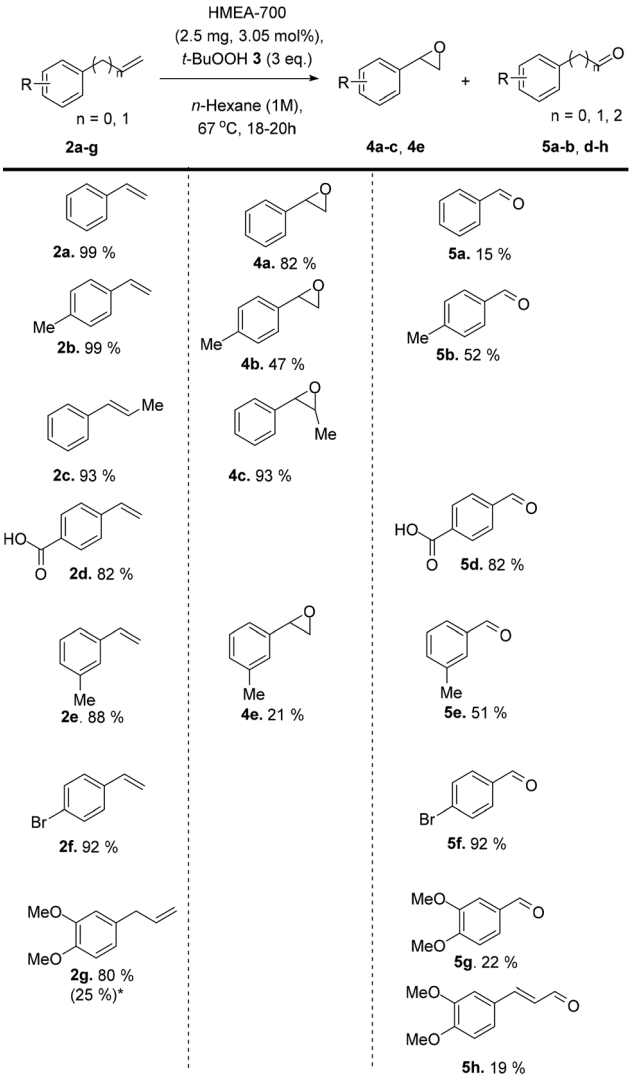

Fig. 9 Scope of the HMEA-700 catalysed oxidative cleavage of alkenes. Conversion (**2**) and yields (**4** and **5**) calculated by GC, using *n*-dodecane as an internal standard. Conditions: 1 mmol alkene **2**, 3 eq. of *t*-BuOOH **3**, 1 mL hexane, 2.5 mg HMEA-700 (3.05 mol%), 67 °C, and 18–20 h. *Unidentified oxidative products.

catalyst approaches 30 in some cases (the TON is calculated as moles of **4a** produced/moles metal atoms). Other styrene derivatives proved to be reactive, but a complex mixture of oxidative breaking products was obtained under the catalytic reaction conditions (Fig. S21). Moreover, an alkyl alkene such as 7-tetradecene was also tested under these reaction conditions, obtaining a mixture of oxidative breaking compounds in the presence of the HMEA catalyst (Fig. S22). H_2O_2 was tested as an oxidation agent and it was found unreactive either with the HMEA-700 catalyst or not (Fig. S23).

Comparison of the HMEA-700 catalyst with the individually supported monometallic catalysts

To demonstrate the potential synergic effect of FeCoNiMn NPs of HMEA-700 in the catalytic oxidative cleavage, monometallic

Table 1 Comparison of oxidative cleavage catalysed by HMEA-700 and monometallic carbon-supported metal NPs with 5 equivalents of *t*-BuOOH. Conversion (**2a**) and yields (**4a** and **5a**) calculated by GC, using *n*-dodecane as an internal standard. Conditions: 1 mmol styrene **2a**, 5 equiv. of *t*-BuOOH **3**, and 1 mL hexane. Turnover number (TON) considers all metal atoms in the NPs

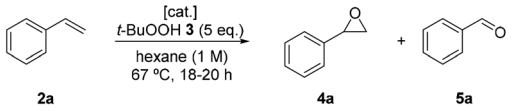

		Metal load (mol%)						Yield (%)		
Entry	Catalyst	Mn	Co	Fe	Ni	Zn	Conv.	**4a**	**5a**	TON
1	HMEA-700	0.65	0.8	0.8	0.8	—	>99	80	20	33
2	Mn (C)	0.65	—	—	—	—	96	86	10	147
3	Co (C)	—	0.8	—	—	—	>99	85	15	124
4	Fe (C)	—	—	0.8			63	58	5	78
5	Ni (C)	—	—	—	0.75	—	49	45	4	65
6	Zn (C)	—	—	—	—	0.4	52	48	4	130

Table 2 Comparison of oxidative cleavage catalysed by HMEA-700, Mn(C), Co(C) and the physical mixture of all individual metals with 3 equivalents of *t*-BuOOH. Conversion (**2a**) and yield (**4a** and **5a**) calculated by GC, using *n*-dodecane as an internal standard. Conditions: 1 mmol styrene **2a**, 3 equiv. of *t*-BuOOH **3**, and 1 mL hexane. Zn is not shown since it is absent. Turnover number (TON) considers all metal atoms in the NPs

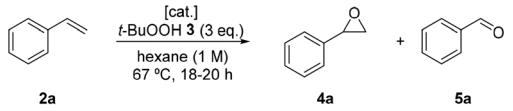

		Metal load (mol%)					Yield (%)		
Entry	Catalyst	Mn	Co	Fe	Ni	Conv. (%)	**4a**	**5a**	TON
1	HMEA-700	0.65	0.8	0.8	0.8	97	82	15	31
2	Mn (C)	0.65	—	—	—	72	65	7	111
3	Co (C)	—	0.8	—	—	88	74	14	100
4	Mn + Co + Fe + Ni (C)	0.65	0.8	0.8	0.8	97	80	17	31

carbon-supported catalysts with Mn, Co, Ni, Fe and even Zn were prepared by impregnation methods (see Fig. S10, S24–27 for characterization) and tested as catalysts. Table 1 shows that, for the oxidative cleavage of styrene **2** with a metal loading of HMEA-700 = 3.05 mol% and with a large excess of *t*-BuOOH **3** (5 equiv.), the monometallic-carbon materials of Fe, Ni and Zn showed yields under 63%, while Mn, Co and HMEA-700 materials exhibited a better performance with yields over 96%.

These results indicate that the monometallic catalysts, considered individually, perform better than the HMEA-700 catalyst, particularly if TONs are considered (considering all metal atoms in the NPs). However, taking into account that the HMEA-700 catalyst requires much less solid than the combination of individual supported metals to be added into the reaction mixture, this has obvious physical advantages for HMEA-700 (with 97% yield) with respect to the physical combination of all individual metals, but not to the Co and Mn materials (88% and 72% yield, respectively), as shown in Table 2. The same result was obtained with 1.5 equivalents of *t*-BuOOH **3** (Fig. S28).

Experimental

Synthesis of MOF 1

The synthesis of MOF **1** was performed after modifying a previously reported procedure.[61] Briefly, 1 mmol of each metal salt: $Co(NO_3)_2{\cdot}6H_2O$, $Ni(NO_3)_2{\cdot}6H_2O$, $Zn(NO_3)_2{\cdot}6H_2O$, $Mn(NO_3)_2{\cdot}4H_2O$, $Fe(SO_4)$ or $FeCl_2$, and 2.5 mmol of the organic linker 2,5-dihydroxyterephthalic acid (H_4DOT) were dissolved in 60 mL of DMF/EtOH/water (in a 15 : 1 : 1 v : v ratio, respectively) and heated to 120 °C for 20–24 h in an autoclave. The resulting crystals were washed 3 times with 50 mL of fresh DMF solvent, and soaked in MeOH for solvent exchange (3 exchanges over a 3 day period). The resulting material was then activated under vacuum (100–200 mTorr) overnight at 80 °C, to remove all the solvent.

Synthesis of the supported HMEA-NPs

A portion of MOF **1** was transferred to the quartz tube reactor and connected to a vertical calcination oven equipped with a N_2 inlet. The gas flow was set up at 100 mL min^{-1} for each experiment. The temperature and heating ramp were adjusted

separately, and the same sample of the material was pyrolyzed at different temperatures 400 °C (5 °C min^{-1}), 550 °C (5 °C min^{-1}), 700 °C (5 °C min^{-1}) and 800 °C (10 °C min^{-1}) for 5 h. Pyrolysis at all temperatures except 800 °C was followed by reduction with H_2 (100 mL min^{-1}) at 400 °C for 4 h. After each pyrolysis, a small portion of the material was separated and saved for further characterization, in order to follow the morphological changes.

Synthesis of metal–C–NPs

A round bottom flask containing one of the selected nitrate salts, $Mn(NO_3)_2{\cdot}4H_2O$, $Co(NO_3)2{\cdot}6H_2O$, $Ni(NO_3)_2{\cdot}6H_2O$, $Fe(NO_3)_3{\cdot}9H_2O$ or $Zn(NO_3)_2{\cdot}6H_2O$ (1.8 mmol), and methanol (50 mL) was placed in an ultrasonic bath for 5 minutes. Active carbon (1 g) was added, and the suspension was sonicated for 2 h at rt. Then, methanol was removed on a rotary evaporator, adjusting the bath temperature at 40 °C. The solid was transferred to a crystallizing dish and dried at 100 °C for 12 h. Then, the reaction mixture was cooled down to room temperature and ground to a powder. The powder was placed in a quartz glass tube reactor and connected to a vertical reduction oven. The reactor was flushed with N_2 for 10 min and then reduced with H_2 (100 mL min^{-1}) at 400 °C for 4 h (heating ramp: 5 °C min^{-1}). The as-prepared carbon-supported catalytic materials were characterized by ICP–OES and powder X-ray diffraction.

General procedure for the oxidative cleavage of styrene derivatives catalysed by HMEA-700 NPs

Typically, a styrene derivative **2** (1 mmol), hexane (1 mL, 1 M) and HMEA-700 (2.5 mg) are placed in a reactor flask containing a stirring bar. Then, *tert*-butyl hydroperoxide **3** solution (5.0–6.0 M in *n*-decane, 3 mmol) is added, and the reaction mixture is stirred in a pre-heated oil bath or a steel block at 67 °C (or the desired temperature for the calculation of the activation energy) for 18 h. Distilled water is added to quench the reaction mixture, and the mixture is extracted with diethyl ether and filtered if necessary. The products are analysed by GC, GC–MS and ^1H NMR in order to determine the structure. The GC conversion is calculated from the loss of the starting material compared to an internal standard (*n*-dodecane) at time = 0 s, and also when finishing the reaction. The yields of each product are calculated by GC, considering the response factors calculated for, for instance, styrene, styrene oxide and benzaldehyde (Fig. S28).

Conclusions

Well-defined high- and medium-entropy alloy NPs were successfully obtained by the pyrolysis of a multi-metallic MOF at 700 °C under an inert atmosphere (N_2). The examination of the morphological changes during the pyrolysis treatment at different temperatures (400 °C, 550 °C, 700 °C and 800 °C) showed that the particle size and distribution can be controlled by adjusting the experimental conditions. The composition of the NPs strongly resembles the pristine MOF's crystal composition, also preserving the original shape. A temperature of 700 °C was optimal, with uniformly dispersed alloy NPs of narrow size distribution (~10 nm), combining 4 transition metals (Fe, Ni, Co, and Mn) in one alloy NP. These structural characteristics reflect on its catalytic performance,[81–84] and the solid material catalyses the oxidative cleavage of alkenes with good yields and is reusable for 10 times. Despite their monometallic counterparts also being capable of efficiently catalysing the reaction, with higher TONs than the HMEA, the results here indicate that stable HMEA nanoalloyed particles supported on a carbonaceous material can be prepared from MOFs in a particle-to-particle fashion and be used as efficient and recyclable catalysts in a relatively complex organic reaction,[85,86] with future potential application in other relatively complex organic reactions and also in the field of electrocatalysis.

Author contributions

A. N., A. L.-T. and A. S.-M. synthesized and characterized the materials. J. O.-M. and M. A. v. S. designed and performed the *in situ* characterization of the materials. A. L.-T. conducted the catalytic and kinetic experiments. A. S.-M conducted the catalytic experiments with monometallic materials. A. L.-P. conceived the idea and supervised the project. All authors contributed to the discussion, participated in the writing of the original draft, and revised the manuscript.

Conflicts of interest

There are no conflicts to declare.

Data availability

Supplementary information (SI): supplemental experimental procedures, Tables S1–S4, and Fig. S1–S28. See DOI: https://doi.org/10.1039/d5nr04879f.

The new HMEA materials are available upon reasonable request. The data that support the plots within this paper, and other findings of this study, are available from the corresponding authors upon reasonable request.

Acknowledgements

Financial support by project PID2023-148441NB-I00 and Severo Ochoa centre of excellence program (CEX2021-001230-S) is gratefully acknowledged. This work has also been funded by Generalitat Valenciana, Grupos Emergentes (GV/2021/138), with the support of Diamond Light Source, instrument B07c (proposal cm28149). A. L.-T. thanks the MICINN for the concession of the FPI grant PRE2020-093338 (through SEV-2016-

0683-20-3). J. O.-M. acknowledges the Ramon y Cajal program for the concession of a contract (RYC2022-036154-I).

References

1 R. E. Hummel, The Bronze Age, in *Understanding Materials Science*, Springer, New York, NY, 2004, pp. 66–73.
2 B. Cantor, I. T. H. Chang, P. Knight and A. J. B. Vincent, *Mater. Sci. Eng. A*, 2004, **375–377**, 213–218.
3 J.-W. Yeh, S.-K. Chen, S.-J. Lin, J.-Y. Gan, T.-S. Chin, T.-T. Shun, C.-H. Tsau and S.-Y. Chang, *Adv. Eng. Mater.*, 2004, **6**, 299–303.
4 H. Zhou, G. Zhu, S. Dong, P. Liu, Y. Lu, Z. Zhou, S. Cao, Y. Zhang and H. Pang, *Adv. Mater.*, 2023, **35**, 2211523.
5 Y. Tang, J. Ding, W. Zhou, S. Cao, F. Yang, Y. Sun, S. Zhang, H. Xue and H. Pang, *Adv. Sci.*, 2023, **10**, 2206960.
6 G. Yuan, Y. Su, X. Zhang, B. Gao, J. Hu, Y. Sun, W. Li, Z. Zhang, M. Shakouri and H. Pang, *Natl. Sci. Rev.*, 2024, **11**, nwae336.
7 C.-Y. Wu, Y.-C. Hsiao, Y. Chen, K.-H. Lin, T.-J. Lee, C.-C. Chi, J.-T. Lin, L.-C. Hsu, H.-J. Tsai, J.-Q. Gao, C.-W. Chang, I.-T. Kao, C.-Y. Wu, Y.-R. Lu, C.-W. Pao, S.-F. Hung, M.-Y. Lu, S. Zhou and T.-H. Yang, *Sci. Adv.*, 2024, **10**, eadl3693.
8 D. B. Miracle and O. N. Senkov, *Acta Mater.*, 2017, **122**, 448–511.
9 W. Zhang, P. K. Liaw and Y. Zhang, *Sci. China Mater.*, 2018, **61**, 2–22.
10 E. P. George, D. Raabe and R. O. Ritchie, *Nat. Rev. Mater.*, 2019, **4**, 515–534.
11 D. B. Miracle, J. D. Miller, O. N. Senkov, C. Woodward, M. D. Uchic and J. Tiley, *Entropy*, 2014, **16**, 494–525.
12 O. N. Senkov, G. B. Wilks, D. B. Miracle, C. P. Chuang and P. K. Liaw, *Intermetallics*, 2010, **18**, 1758–1765.
13 O. N. Senkov, G. B. Wilks, J. M. Scott and D. B. Miracle, *Intermetallics*, 2011, **19**, 698–706.
14 Y. Zhou, M. Wang, L. Zhang, N. Li, T. Qian, C. Yan and J. Lu, *ACS Nano*, 2025, **19**, 7273–7282.
15 X. Li, Z. Xie, S. Roy, L. Gao, J. Liu, B. Zhao, R. Wei, B. Tang, H. Wang, P. Ajayan and K. Tang, *Adv. Mater.*, 2025, **37**, 2410295.
16 H. Cai, H. Yang, S. He, D. Wan, Y. Kong, D. Li, X. Jiang, X. Zhang, Q. Hu and C. He, *Angew. Chem., Int. Ed.*, 2025, **64**, e202423765.
17 Y. Xin, S. Li, Y. Qian, W. Zhu, H. Yuan, P. Jiang, R. Guo and L. Wang, *ACS Catal.*, 2020, **10**, 11280–11306.
18 G. M. Tomboc, T. Kwon, J. Joo and K. J. Lee, *Mater. Chem. A*, 2020, **8**, 14844–14862.
19 Y. Yao, Z. Huang, P. Xie, S. D. Lacey, R. J. Jacob, H. Xie, F. Chen, A. Nie, T. Pu, M. Rehwoldt, D. Yu, M. R. Zachariah, C. Wang, R. Shahbazian-Yassar, J. Li and L. Hu, *Science*, 2018, **359**, 1489–1494.
20 S. Gao, S. Hao, Z. Huang, Y. Yuan, S. Han, L. Lei, X. Zhang, R. Shahbazian-Yassar and J. Lu, *Nat. Commun.*, 2020, **11**, 2016.
21 M. Y. Rekha, N. Mallik and C. Srivastava, *Sci. Rep.*, 2018, **8**, 8737.
22 A. Mao, H. Xiang, X. Ran, Y. Li, X. Jin, H. Yu and X. Gu, *J. Alloys Compd.*, 2019, **775**, 1177–1183.
23 K. Li and W. Chen, *Today Energy*, 2021, **20**, 100638.
24 J. Chen, J. Ma, T. Huang, Q. Liu, X. Liu, R. Luo, J. Xu, X. Wang, T. Jiang, H. Liu, Z. Lv, T. Yao, G. Wang, X. Zheng, Z. Li and W. Chen, *Angew. Chem., Int. Ed.*, 2025, e202503330.
25 A. Dhakshinamoorthy, S. Navalon, A. Primo and H. Garcia, *Angew. Chem., Int. Ed.*, 2024, **63**, e202311241.
26 A. Dhakshinamoorthy, A. M. Asiri and H. Garcia, *Chem. – Eur. J.*, 2023, **29**, e202204016.
27 E. Tiburcio, Y. Zheng, C. Bilanin, J. C. Hernández-Garrido, A. Vidal-Moya, J. Oliver-Meseguer, N. Martín, M. Mon, J. Ferrando-Soria, D. Armentano, E. Pardo and A. Leyva-Pérez, *J. Am. Chem. Soc.*, 2023, **145**, 10342–10354.
28 J. Ballesteros-Soberanas, N. Martín, M. Bacic, E. Tiburcio, M. Mon, J. C. Hernández-Garrido, C. Marini, M. Boronat, J. Ferrando-Soria, D. Armentano, E. Pardo and A. Leyva-Pérez, *Nat. Catal.*, 2024, **7**, 452–463.
29 H. D. Mai, K. Rafiq and H. Yoo, *Chem. – Eur. J.*, 2017, **23**, 5631–5651.
30 B. Y. Guan, Y. Lu, Y. Wang, M. Wu and X. W. Lou, *Adv. Funct. Mater.*, 2018, **28**, 1706738.
31 B. Y. Guan, Y. Lu and X. W. Lou, *Energy Environ. Sci.*, 2016, **9**, 3092–3096.
32 H. B. Wu and X. W. Lou, *Sci. Adv.*, 2023, **3**, eaap9252.
33 M. H. Yap, K. L. Fow and G. Z. Chen, *Green Energy Environ.*, 2017, **2**, 218–245.
34 A. Bavykina, N. Kolobov, I. S. Khan, J. A. Bau, A. Ramirez and J. Gascon, *Chem. Rev.*, 2020, **120**, 8468–8535.
35 B. Liu, H. Shioyama, T. Akita and Q. Xu, *J. Am. Chem. Soc.*, 2008, **130**, 5390–5391.
36 Q.-X. Luo, L.-P. Guo, S.-Y. Yao, J. Bao, Z.-T. Liu and Z.-W. Liu, *J. Catal.*, 2019, **369**, 143–156.
37 S. Mandegarzad, J. B. Raoof, S. R. Hosseini and R. Ojani, *Electrochim. Acta*, 2016, **190**, 729–736.
38 S. Abednatanzi, P. G. Derakhshandeh, H. Depauw, F.-X. Coudert, H. Vrielinck, P. Van Der Voort and K. Leus, *Chem. Soc. Rev.*, 2019, **48**, 2535–2565.
39 J. Deng, P. Ren, D. Deng and X. Bao, *Angew. Chem., Int. Ed.*, 2015, **54**, 2100–2104.
40 X. Zheng, J. Deng, N. Wang, D. Deng, W.-H. Zhang, X. Bao and C. Li, *Angew. Chem., Int. Ed.*, 2014, **53**, 7023–7027.
41 J. Long, K. Shen, L. Chen and Y. Li, *J. Mater. Chem. A*, 2016, **4**, 10254–10262.
42 H. Wang, X. Li, X. Lan and T. Wang, *ACS Catal.*, 2018, **8**, 2121–2128.
43 Z.-F. Huang, J. Song, K. Li, M. Tahir, Y.-T. Wang, L. Pan, L. Wang, X. Zhang and J.-J. Zou, *J. Am. Chem. Soc.*, 2016, **138**, 1359–1365.
44 C. Feng, Y. Guo, Y. Xie, X. Cao, S. Li, L. Zhang, W. Wang and J. Wang, *Nanoscale*, 2020, **12**, 5942–5952.
45 F. Tang, L. Wang, M. D. Walle, A. Mustapha and Y.-N. Liu, *J. Catal.*, 2020, **383**, 172–180.

46 Y. Yao, Q. Dong, A. Brozena, J. Luo, J. Miao, M. Chi, C. Wang, I. G. Kevrekidis, Z. J. Ren, J. Greeley, G. Wang, A. Anapolsky and L. Hu, *Science*, 2022, **376**, eabn3103.
47 N. Zhang, X. Chen, S. Liu, J. Meng, M. Armbrüster and C. Liang, *ACS Appl. Mater. Interfaces*, 2023, **15**(19), 23276–23285.
48 J. Ma, F. Xing, Y. Nakaya, K. Shimizu and S. Furukawa, *Angew. Chem., Int. Ed.*, 2022, **61**, e202200889.
49 H. Liu, L. Zhang, K. Wang, L. Wang, L. Zhang, B. Yu and F. Yang, *J. Phys. Chem. C*, 2023, **127**, 7211–7219.
50 S. H. Albedwawi, A. AlJaberi, G. N. Haidemenopoulos and K. Polychronopoulou, *Mater. Des.*, 2021, **202**, 109534.
51 Y. Wang, J. Mi and Z.-S. Wu, *Chem Catal.*, 2022, **2**, 1624–1656.
52 Y. Pan, J.-X. Liu, T.-Z. Tu, W. Wang and G.-J. Zhang, *Chem. Eng. J.*, 2023, **451**, 138659.
53 C. Deng, T. Wang, P. Wu, W. Zhu and S. Dai, *Nano Energy*, 2024, **120**, 109153.
54 L. Sun, K. Wen, G. Li, X. Zhang, X. Zeng, B. Johannessen and S. Zhang, *ACS Mater. Au*, 2024, **4**, 547–556.
55 X. Han, G. Wu, S. Zhao, J. Guo, M. Yan, X. Hong and D. Wang, *Matter*, 2023, **6**, 1717–1751.
56 C. Zhan, L. Bu, H. Sun, X. Huang, Z. Zhu, T. Yang, H. Ma, L. Li, Y. Wang, H. Geng, W. Wang, H. Zhu, C.-W. Pao, Q. Shao, Z. Yang, W. Liu, Z. Xie and X. Huang, *Angew. Chem., Int. Ed.*, 2023, **62**, e202213783.
57 J.-T. Ren, L. Chen, H.-Y. Wang and Z.-Y. Yuan, *Chem. Soc. Rev.*, 2023, **52**, 8319–8373.
58 Y. Xu, W. Yuan, C. Geng, Z. Hu, Q. Li, Y. Zhao, X. Zhang, Z. Zhou, C. Yang and Q.-H. Yang, *Adv. Sci.*, 2024, **11**, 2402497.
59 M. K. Plenge, J. K. Pedersen, A. Bagger and J. Rossmeisl, *J. Catal.*, 2024, **430**, 115322.
60 T. A. A. Batchelor, J. K. Pedersen, S. H. Winther, I. E. Castelli, K. W. Jacobsen and J. Rossmeisl, *Joule*, 2019, **3**, 834–845.
61 L. J. Wang, H. Deng, H. Furukawa, F. Gándara, K. E. Cordova, D. Peri and O. M. Yaghi, *Inorg. Chem.*, 2014, **53**, 5881–5883.
62 A. Tayal, Y. Chen, C. Song, S. Hiroi, L. S. R. Kumara, N. Palina, O. Seo, M. Mukoyoshi, H. Kobayashi, H. Kitagawa and O. Sakata, *Inorg. Chem.*, 2018, **57**, 10072–10080.
63 K. W. Golub, T. P. Sulmonetti, L. A. Darunte, M. S. Shealy and C. W. Jones, *ACS Appl. Nano Mater.*, 2019, **2**, 6040–6056.
64 L. Huang, M. Liu, H. Lin, Y. Xu, J. Wu, V. P. Dravid, C. Wolverton and C. A. Mirkin, *Science*, 2019, **365**, 1159–1163.
65 H. Hirakata, K. Sano and T. Shimada, *Appl. Phys. Lett.*, 2020, **116**, 111902.
66 S. Choi, J. Lee, M. Pin, J.-H. Kwon, I. Kim, M. S. Yeom, C. S. Kim, H. S. Lee, S. J. Ahn, S.-H. Yi and Y. H. Kim, *Nanoscale*, 2019, **11**, 6685–6692.
67 P. Liang, Q. Wang, J. Kang, W. Tian, H. Sun and S. Wang, *Chem. Eng. J.*, 2018, **351**, 641–649.
68 K. Koo, B. Shen, S.-I. Baik, Z. Mao, P. J. M. Smeets, I. Cheuk, K. He, R. dos Reis, L. Huang, Z. Ye, X. Hu, C. A. Mirkin and V. P. Dravid, *Nat. Commun.*, 2023, **14**, 3790.
69 S. Moniri, Y. Yang, J. Ding, Y. Yuan, J. Zhou, L. Yang, F. Zhu, Y. Liao, Y. Yao, L. Hu, P. Ercius and J. Miao, *Nature*, 2023, **624**, 564–569.
70 H. Tan, X. Li, X. Dong, W. Zhong, T. Zhan, Y. Qiao, H. Ma, J. Teng and J. Zhu, *Fuel Process. Technol.*, 2024, **254**, 108045.
71 M. Athariboroujeny, A. Raub, V. Iablokov, S. Chenakin, L. Kovarik and N. Kruse, *ACS Catal.*, 2019, **9**, 5603–5612.
72 E. Tiburcio, R. Greco, M. Mon, J. Ballesteros-Soberanas, J. Ferrando-Soria, M. López-Haro, J. C. Hernández-Garrido, J. Oliver-Meseguer, C. Marini, M. Boronat, D. Armentano, A. Leyva-Pérez and E. Pardo, *J. Am. Chem. Soc.*, 2021, **143**, 2581–2592.
73 R. Greco, E. Tiburcio-Fortes, A. Fernandez, C. Marini, A. Vidal-Moya, J. Oliver-Meseguer, D. Armentano, E. Pardo, J. Ferrando-Soria and A. Leyva-Pérez, *Chem. – Eur. J.*, 2022, **28**, e202103781.
74 C. Negro, C. Bilanin, X. Qu, J. Oliver-Meseguer, J. Ferrando-Soria, A. Leyva-Pérez, D. Armentano and E. Pardo, *Chem. Commun.*, 2022, **58**, 5578–5581.
75 S. Hervàs-Arnandis, F. Garnes-Portolés, S. Rodríguez-Nuévalos, J. Oliver-Meseguer and A. Leyva-Pérez, *Nat. Commun.*, 2025, **16**, 6542.
76 C. Annese, D. Caputo, L. D'Accolti, C. Fusco, A. Nacci, A. Rossin, G. Tuci and G. Giambastiani, *Eur. J. Inorg. Chem.*, 2019, **2**, 221–229.
77 J.-Q. Yu and E. J. Corey, *Org. Lett.*, 2002, **4**, 2727–2730.
78 M. Fadhli, I. Khedher and J. M. Fraile, *C. R. Chim.*, 2017, **20**, 827–832.
79 M. Bačić, J. Oliver-Meseguer and A. Leyva-Pérez, *Appl. Catal., A*, 2024, **674**, 119632.
80 A. Lumbreras-Teijeiro, J. Oliver-Meseguer and A. Leyva-Pérez, *ChemPlusChem*, 2025, 2500203.
81 A. Leyva-Perez, J. Oliver-Meseguer, J. R. Cabrero-Antonino, P. Rubio-Marques, P. Serna, S. I. Al-Resayes and A. Corma, *ACS Catal.*, 2013, **3**, 1865–1873.
82 J. Oliver-Meseguer, M. Boronat, A. Vidal-Moya, P. Concepción, M. á. Rivero-Crespo, A. Leyva-Pérez and A. Corma, *J. Am. Chem. Soc.*, 2018, **140**, 3215–3218.
83 M. Su, Y. Su, Y. Wang, M. Cui, H. Zheng, S. Shahid, J. S. A. Owusu, W. Deng, B. Zhao and J. Zuwała, *ACS Catal.*, 2025, **15**, 18493–18510.
84 P. Qiu, Z. Fang, L. Yuan, J. Hou, J. Zhu, C. Ke, L. Zhang and X. Zhuang, *ChemCatChem*, 2025, **17**, e00454.
85 E. Reale, A. Leyva, A. Corma, C. Martínez, H. García and F. Rey, *J. Mater. Chem.*, 2005, **15**, 1742–1754.
86 M. Mon, R. Bruno, S. Sanz-Navarro, C. Negro, J. Ferrando-Soria, L. Bartella, L. D. Donna, M. Prejanò, T. Marino, A. Leyva-Pérez, D. Armentano and E. Pardo, *Nat. Commun.*, 2020, **11**, 3080.

